Constrained interpolation profile conservative semi-Lagrangian scheme based on third-order polynomial functions and essentially non-oscillatory (CIP-CSL3ENO) scheme

Qijie Li[1], Syazana Omar[1], Xi Deng[1,2], Kensuke Yokoi[1*]
[1]School of Engineering, Cardiff University, Cardiff, CF24 3AA, UK
[2]Department of Energy Sciences, Tokyo Institute of Technology, Yokohama, 226-8502, Japan

January 4, 2017

Abstract

We propose a fully conservative and less oscillatory multi-moment scheme for the approximation of hyperbolic conservation laws. The proposed scheme (CIP-CSL3ENO) is based on two CIP-CSL3 schemes and the essentially non-oscillatory (ENO) scheme. In this paper, we also propose an ENO indicator for the multi-moment framework, which intentionally selects non-smooth stencil but can efficiently minimize numerical oscillations. The proposed scheme is validated through various benchmark problems and a comparison with an experiment of two droplets collision/separation. The CIP-CSL3ENO scheme shows approximately fourth-order accuracy for smooth solution, and captures discontinuities and smooth solutions simultaneously without numerical oscillations for solutions which include discontinuities. The numerical results of two droplets collision/separation (3D free surface flow simulation) show that the CIP-CSL3ENO scheme can be applied to various types of fluid problems not only compressible flow problems but also incompressible and 3D free surface flow problems.

1 Introduction

In this paper, we propose a less oscillatory multi-moment method for the approximation of hyperbolic conservation laws

$$\frac{\partial \phi}{\partial t} + \frac{\partial (u\phi)}{\partial x} = 0, \tag{1}$$

where ϕ is the scalar and u is the velocity. The proposed method is based on the constrained interpolation profile-conservative semi-Lagrangian (CIP-CSL) scheme [21, 27, 25, 12] and the essentially non-oscillatory (ENO) scheme [3, 17, 18, 16].

The CIP-CSL scheme is a solver of conservation laws based on a multi-moment concept which uses cell average and boundary value as moments (variables), and has been applied to various types of fluid problems [22, 24, 23] including interfacial flows such as droplet splashing [29, 30]. There are several variants of the CIP-CSL scheme such as CIP-CSL2 (CIP-CSL with second-order polynomial function) [27] and CIP-CSL3 (CIP-CSL with third-order polynomial function) [25]. In CSL2 which is based on a second-order polynomial interpolation function, three moments within the upwind cell (i.e. a cell average and two boundary values) are used for the interpolation function as shown in Fig. 1 (a). In CSL3 which is based on a third-order polynomial

*Corresponding author: Postal address: School of Engineering, Cardiff University, The Parade, Cardiff, CF24 3AA, UK, Tel. +44-29-20870844, Fax. +44-29-20874716, YokoiK@cardiff.ac.uk.

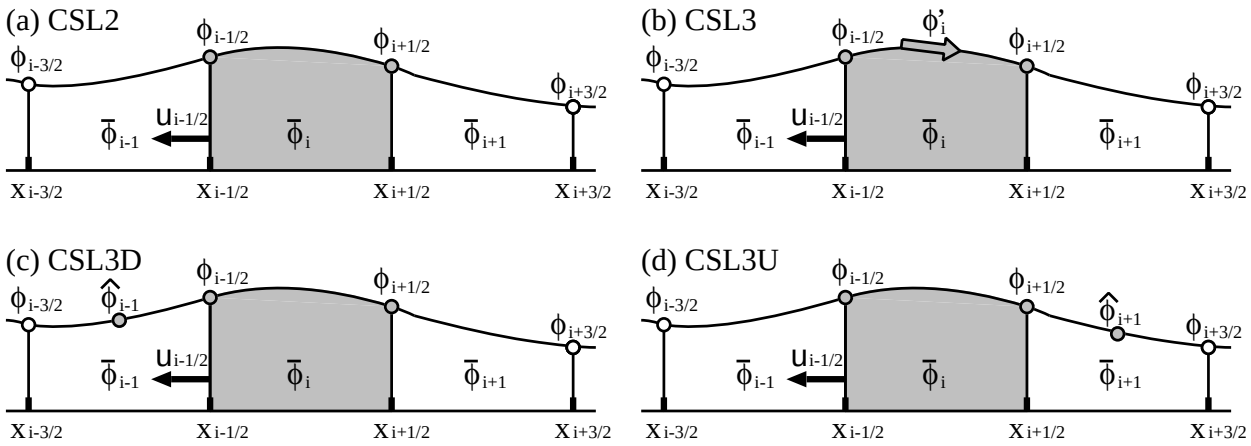

Figure 1: Schematic figures of the CIP-CSL2 method (a), the CIP-CSL3 method (b), the CIP-CSL3D method (c) and the CIP-CL3U method (d). $u_{i-1/2} < 0$ is assumed. The moments which are indicated by gray color are used as constraints to construct interpolation functions $\Phi_i^{CSL2}(x)$, $\Phi_i^{CSL3}(x)$, $\Phi_i^{CSL3D}(x)$ and $\Phi_i^{CSL3U}(x)$.

interpolation function, a derivative at cell center is used as an additional constraint as shown in Fig. 1 (b). The derivative is a control parameter and mainly used as a limiter. Recently the CIP-CSL3D scheme (D of CSL3D stands for Downwind) was proposed [12]. Although CSL3D also uses a third-order polynomial interpolation function like CSL3, a moment in the downwind cell is used as the additional constraint instead of the derivative in CSL3 (Fig. 1 (c)). In this paper, we propose another variant of CSL3, which will be called CSL3U and which uses an additional moment in upwind side instead of a moment in the downwind cell of CIP-CSL3D (U of CSL3U stands for Upwind) as shown in Fig. 1 (d). By combining CSL3U and CSL3D using the idea of the ENO scheme, we develop a less oscillatory CSL3 (hereinafter referred to as CIP-CSL3ENO scheme). The CIP-CSL3ENO scheme maintains approximately fourth-order accuracy unlike CSL3 schemes which use a standard limiter. Although a less oscillatory formulation of CSL3D (CSL3DL) has been proposed in [12], the formulation is using a type of limiter so that the order of accuracy is much lower than the CIP-CSL3ENO scheme. CSL3DL also involves several parameters which are empirically determined. On the other hand, the CIP-CSL3ENO scheme is free from such parameters.

The ENO scheme was invented by Harten et al. [3] in 1987. The ENO scheme as well as weighted ENO (WENO) scheme [11, 10, 13] has been designed for problems which include both smooth and discontinuous solutions. The key idea of the ENO scheme is the use of adaptive stencils. The ENO scheme selects an appropriate stencil (typically the smoothest stencil) to avoid crossing discontinuities in the interpolation procedure as much as possible. The ENO scheme has been improved by many researchers [17, 18, 16, 14, 4]. In this paper, ENO and CIP-CSL3 schemes are combined to develop a less oscillatory CSL3 scheme. Although there are some previous work which combined WENO and a multi-moment method [5, 20], these are using different approaches. In [5], 5th-order multi-moment WENO scheme was proposed. In this paper, we proposed a 4th-order scheme which is based on shorter stencils. Their reconstruction approaches are quite different with the proposed scheme. In [20], WENO was used as the slope limiter and was combined with a different multi-moment method which is called the multi-moment constrained finite volume (MCV) method [8]. In the proposed scheme, the ENO scheme is directly applied to the interpolation function (not through a slope limiter).

2 Numerical method

In this section, we propose the CIP-CSL3U and CIP-CSL3ENO schemes after the CIP-CSL2, CIP-CSL3 and CIP-CSL3D schemes are briefly explained. The CIP-CSL3ENO scheme is based on the CIP-CSL3D method and newly proposed CIP-CSL3U method, and can minimize numerical oscillation by selecting an appropriate stencil (CSL3D or CSL3U).

2.1 CIP-CSL2

The CIP-CSL2 scheme is based on the following second-order polynomial interpolation function

$$\Phi_i^{CSL2}(x) = C_{2,i}^{CSL2}(x - x_{i-1/2})^2 + C_{1,i}^{CSL2}(x - x_{i-1/2}) + C_{0,i}^{CSL2}. \tag{2}$$

The coefficients ($C_{2,i}^{CSL2}$, $C_{1,i}^{CSL2}$ and $C_{0,i}^{CSL2}$) are determined by using three constraints ($\bar{\phi}_i$, $\phi_{i-1/2}$ and $\phi_{i+1/2}$) which are indicated in Fig. 1 (a) (for more details, see [27]). By using the interpolation function, the cell average $\bar{\phi}_i$ and boundary value $\phi_{i-1/2}$ are updated by a third-order TVD Runge-Kutta formulation [15, 7] based on the CSL formulation.

In the third-order TVD Runge-Kutta formulation, we solve the following initial value problem

$$\frac{\partial X}{\partial t} = -u(X,t), \tag{3}$$

$$X_0 = x_{i-1/2},$$

using the third-order TVD Runge-Kutta method as follows,

$$X_1 = X_0 - u(X_0,t_0)\Delta t, \tag{4}$$

$$X_2 = \frac{3}{4}X_0 + \frac{1}{4}X_1 - \frac{1}{4}u(X_1,t_1)\Delta t, \tag{5}$$

$$X_3 = \frac{1}{3}X_0 + \frac{2}{3}X_2 - \frac{2}{3}u(X_2,t_2)\Delta t. \tag{6}$$

Then using the semi-Lagrangian method, $\phi_{i-1/2}$ at each Runge-Kutta time step can be obtained as follows

$$\phi_{i-1/2}^{<k>} = \begin{cases} \Phi_{i-1}^{CSL2}(X_k) & \text{if} \quad X_k - X_0 \le 0 \\ \Phi_i^{CSL2}(X_k) & \text{if} \quad X_k - X_0 > 0, \end{cases} \tag{7}$$

where k is the Runge-Kutta time step. The boundary value $\phi_{i-1/2}$ is updated by solving the conservation equation of a differential form

$$\frac{\partial \phi}{\partial t} + u\frac{\partial \phi}{\partial x} = -\phi\frac{\partial u}{\partial x}, \tag{8}$$

as follows

$$\phi_{i-1/2}^{n+1} = \phi_{i-1/2}^{<3>} - \frac{\phi_{i-1/2}^{<0>} + \phi_{i-1/2}^{<1>} + 4\phi_{i-1/2}^{<2>}}{6}\frac{\partial u}{\partial x}(X_0)\Delta t. \tag{9}$$

The cell average is updated by a finite volume formulation as follows

$$\bar{\phi}_i^{n+1} = \bar{\phi}_i^n - \frac{F_{i+1/2} - F_{i-1/2}}{\Delta x}, \tag{10}$$

here

$$F_{i-1/2} = \frac{\phi_{i-1/2}^{<0>} + \phi_{i-1/2}^{<1>} + 4\phi_{i-1/2}^{<2>}}{6}u(X_0). \tag{11}$$

2.2 CIP-CSL3 (CSL3CW and CSL3H)

The CIP-CSL3 scheme employs the following third-order polynomial interpolation function

$$\Phi_i^{CSL3}(x) = C_{3,i}^{CSL3}(x-x_{i-1/2})^3 + C_{2,i}^{CSL3}(x-x_{i-1/2})^2 + C_{1,i}^{CSL3}(x-x_{i-1/2}) + C_{0,i}^{CSL3}. \tag{12}$$

These four coefficients ($C_{3,i}^{CSL3}$, $C_{2,i}^{CSL3}$, $C_{1,i}^{CSL3}$, $C_{0,i}^{CSL3}$) are determined by using the same three constrains with CSL2 ($\bar{\phi}_i$, $\phi_{i-1/2}$ and $\phi_{i+1/2}$) and a slope at the cell center in the upwind cell (ϕ_i'), as shown in Fig. 1 (b).

There are some formulations for estimating the slope ϕ'. In a less oscillatory CSL3 formulation which is called CSL3CW [2], ϕ_i' is estimated as

$$\phi_i' = \begin{cases} \min(|\hat{\phi}_{i+1}-\hat{\phi}_{i-1}|, 2|\hat{\phi}_{i+1}-\hat{\phi}_i|, 2|\hat{\phi}_i-\hat{\phi}_{i-1}|)\mathrm{sgn}(\hat{\phi}_{i+1}-\hat{\phi}_{i-1})/\Delta x & \text{if } (\hat{\phi}_{i+1}-\hat{\phi}_i)(\hat{\phi}_i-\hat{\phi}_{i-1}) > 0 \\ 0 & \text{otherwise,} \end{cases} \tag{13}$$

where

$$\hat{\phi}_i = \frac{3}{2}\bar{\phi}_i - \frac{1}{4}(\phi_{i+1/2}+\phi_{i-1/2}). \tag{14}$$

In another CSL3 formulation which is called CSL3HYMAN (hereinafter referred to as CSL3H) [6], ϕ_i' is estimated as

$$\phi_i' = \frac{\hat{\phi}_{i+2}+8\hat{\phi}_{i+1}-8\hat{\phi}_{i-1}-\hat{\phi}_{i-2}}{12\Delta x}. \tag{15}$$

CSL3H has 4th-order accuracy for smooth solutions. However CSL3H is not oscillation free when solutions include discontinuities. For more details, see [25].

2.3 CIP-CSL3D

The CIP-CSL3D scheme is also based on the third-order polynomial interpolation function

$$\Phi_i^{CSL3D}(x) = C_{3,i}^{CSL3D}(x-x_{i-1/2})^3 + C_{2,i}^{CSL3D}(x-x_{i-1/2})^2 + C_{1,i}^{CSL3D}(x-x_{i-1/2}) + C_{0,i}^{CSL3D}. \tag{16}$$

These four coefficients are determined by using the same three constrains with CSL2 ($\bar{\phi}_i$, $\phi_{i-1/2}$ and $\phi_{i+1/2}$) and an interpolated cell center value ($\hat{\phi}_{i-1}$) in the downwind cell, as shown in Fig. 1 (c). Although CSL3D also uses the same cubic interpolation function with CSL3, in CSL3D, all coefficients are determined without any control parameter like CSL2 and unlike CSL3. For more details, see [12].

2.4 CIP-CSL3U

2.4.1 Formulation of CSL3U

We propose the CIP-CSL3U method which is another variant of CSL3. While CSL3D used three constraints in the upwind cell and a constraint in the downwind cell (Fig. 1 (c)), CSL3U employs all four constraints in upwind cells as shown in Fig. 1 (d). For the case of $u_{i-1/2} < 0$, the interpolation function is

$$\Phi_i^{CSL3U}(x) = C_{3,i}^{CSL3U}(x-x_{i-1/2})^3 + C_{2,i}^{CSL3U}(x-x_{i-1/2})^2 + C_{1,i}^{CSL3U}(x-x_{i-1/2}) + C_{0,i}^{CSL3U}. \tag{17}$$

Using the following four constraints

$$\phi_{i-1/2} = \Phi_i^{CSL3U}(x_{i-1/2}),\ \ \bar{\phi}_i = \frac{\int_{x_{i-1/2}}^{x_{i+1/2}} \Phi_i^{CSL3U}(x)dx}{\Delta x},\ \ \phi_{i+1/2} = \Phi_i^{CSL3U}(x_{i+1/2}),\ \ \hat{\phi}_{i+1} = \Phi_i^{CSL3U}(x_{i+1}). \tag{18}$$

The coefficients are obtained as follows

$$C_{3,i}^{CSL3U} = \frac{1}{3\Delta x^3}(-7\phi_{i-1/2}+18\bar{\phi}_i-15\phi_{i+1/2}+4\hat{\phi}_{i+1}), \tag{19}$$

$$C_{2,i}^{CSL3U} = \frac{1}{2\Delta x^2}(13\phi_{i-1/2} - 30\bar{\phi}_i + 21\phi_{i+1/2} - 4\hat{\phi}_{i+1}), \tag{20}$$

$$C_{1,i}^{CSL3U} = \frac{1}{6\Delta x}(-31\phi_{i-1/2} + 54\bar{\phi}_i - 27\phi_{i+1/2} + 4\hat{\phi}_{i+1}), \tag{21}$$

$$C_{0,i}^{CSL3U} = \phi_{i-1/2}. \tag{22}$$

For the case of $u_{i-1/2} \geq 0$, the cubic interpolation function is

$$\Phi_{i-1}^{CSL3U}(x) = C_{3,i-1}^{CSL3U}(x - x_{i-1/2})^3 + C_{2,i-1}^{CSL3U}(x - x_{i-1/2})^2 + C_{1,i-1}^{CSL3U}(x - x_{i-\frac{1}{2}}) + C_{0,i-1}^{CSL3U}. \tag{23}$$

The coefficients are

$$C_{3,i-1}^{CSL3U} = -\frac{1}{3\Delta x^3}(-7\phi_{i-1/2} + 18\bar{\phi}_{i-1} - 15\phi_{i-3/2} + 4\hat{\phi}_{i-2}), \tag{24}$$

$$C_{2,i-1}^{CSL3U} = \frac{1}{2\Delta x^2}(13\phi_{i-1/2} - 30\bar{\phi}_{i-1} + 21\phi_{i-3/2} - 4\hat{\phi}_{i-2}), \tag{25}$$

$$C_{1,i-1}^{CSL3U} = -\frac{1}{6\Delta x}(-31\phi_{i-1/2} + 54\bar{\phi}_{i-1} - 27\phi_{i-3/2} + 4\hat{\phi}_{i-2}), \tag{26}$$

$$C_{0,i-1}^{CSL3U} = \phi_{i-\frac{1}{2}}. \tag{27}$$

2.4.2 Fourier analysis of CSL3U

We conduct a Fourier analysis [9] of newly proposed CSL3U and compare the results with the results of CSL3D. Fourier analysis shows resolution of spatial derivatives in the wavenumber space. The spatial profile of $\Phi(x)$ is defined over the domain $[0, L]$ with a uniform grid spacing Δx, and is decomposed into Fourier series

$$\Phi(x) = \sum_k \Phi(k)\, e^{jwx/\Delta x}, \tag{28}$$

where $j = \sqrt{-1}$, and $w = 2\pi k\Delta x/L$ is the scaled wavenumber. For instance, the point value at $x_{i-1/2}$ is decomposed as

$$\Phi_{i-1/2} = \sum_k \Phi(k)\, e^{jwx_{i-1/2}/\Delta x}. \tag{29}$$

Using Eq.(29), the value at $x_{i-1/2+m}$ is decomposed as

$$\Phi_{i-1/2+m} = \Phi_{i-1/2}\, e^{jwm}. \tag{30}$$

The cell average $\bar{\Phi}_i$ is also decomposed as

$$\bar{\Phi}_i = \frac{1}{\Delta x}\int_0^{\Delta x} \Phi(x_{i-1/2} + x)\, dx = \Phi_{i-1/2}\, \frac{e^{jw/2} - 1}{jw}. \tag{31}$$

Since the equation (31) represents the relationship between the point value and the cell average, accuracy of CSL3U and CSL3D at $x_{i-1/2}$ can be examined by using Eq.(30) and Eq.(31). The same analogy can be used for analysis at x_i and $x_{i+1/2}$. In this analysis, we consider the case of $u_{i-1/2} < 0$ as shown in Fig. 1.

Figures 2, 3 and 4 show the results of Fourier analysis of CSL3U with those of CSL3D at x_i, $x_{i-1/2}$ and $x_{i+1/2}$, respectively. The mathematical formulations are given in Appendix A. As shown in Fig. 2, at the cell center x_i, the results of CSL3U and CSL3D are identical because both schemes are symmetrical at x_i. At $x_{i-1/2}$, CSL3D is consistently superior to CSL3U as shown in Fig. 3. This will be because the additional moment of CSL3D ($\hat{\phi}_{i-1}$) is closer to $x_{i-1/2}$ than that of CSL3U ($\hat{\phi}_{i+1}$). At $x_{i+1/2}$, CSL3U is superior to CSL3D as shown in Fig. 4. The reason will be the same with the above. The results at $x_{i-1/2}$ and $x_{i+1/2}$ are basically symmetrical due to the nature of discretizations.

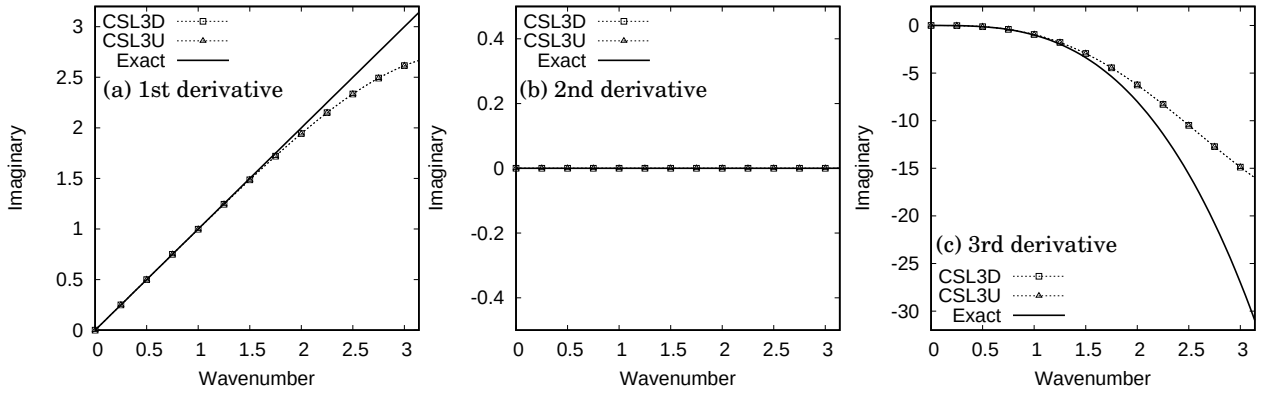

Figure 2: Spatial derivatives of CSL3D and CSL3U at the cell center x_i. (a), (b) and (c) show results of imaginary parts of first, second and third derivatives, respectively.

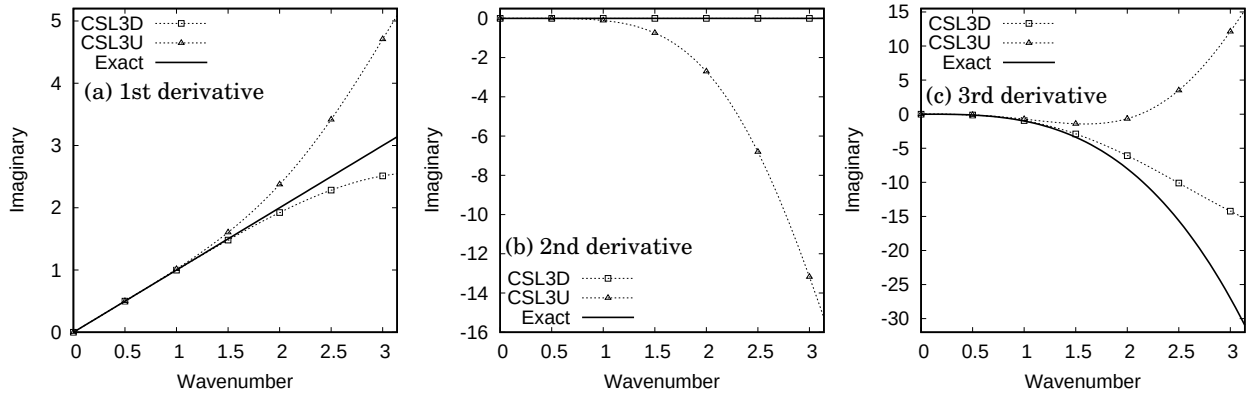

Figure 3: Spatial derivatives of CSL3D and CSL3U at a cell boundary $x_{i-1/2}$. (a), (b) and (c) show results of imaginary parts of first, second and third derivatives, respectively.

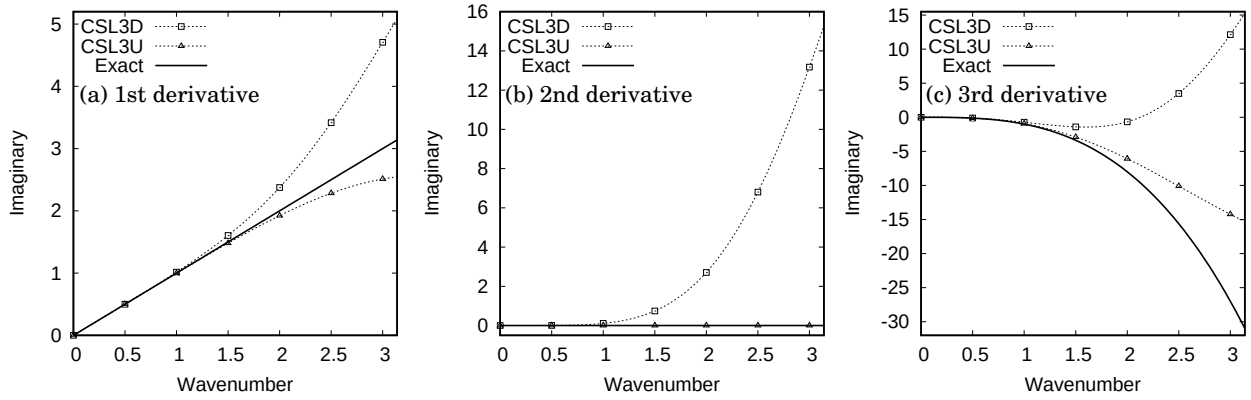

Figure 4: Spatial derivatives of CSL3D and CSL3U at a cell boundary $x_{i+1/2}$. (a), (b) and (c) show results of imaginary parts of first, second and third derivatives, respectively.

2.5 CIP-CSL3ENO

In this subsection, we propose the CIP-CSL3ENO scheme which is based on CSL3D and CSL3U, and the ENO scheme. In CSL3D and CSL3U, three different types of moments (i.e. $\phi_{i-1/2}$, $\bar{\phi}_i$ and $\hat{\phi}_i$) are used. Therefore the design of selector was not simple. Although we tested many possible selectors/indicators, in this paper, we propose a simple and efficient selector based on a type of ratios of successive gradients.

Firstly we consider the case as shown in Fig. 1 (i.e. $u_{i-1/2} < 0$). The smoothness of CSL3D and CSL3U stencils are evaluated using ratios of successive gradients, $r_{i-1/2}$ and $r_{i+1/2}$, respectively. $r_{i-1/2}$ is defined as

$$r_{i-1/2} = \mathrm{sgn}\left(\frac{\hat{\phi}_i - \phi_{i-1/2}}{\phi_{i-1/2} - \hat{\phi}_{i-1}}\right)\max\left(\frac{|\hat{\phi}_i - \phi_{i-1/2}|}{|\phi_{i-1/2} - \hat{\phi}_{i-1}|}, \frac{|\phi_{i-1/2} - \hat{\phi}_{i-1}|}{|\hat{\phi}_i - \phi_{i-1/2}|}\right). \tag{32}$$

We select a stencil by the following selection criteria.
Selection criteria:

1. If both $r_{i-1/2}$ and $r_{i+1/2}$ are negative, the larger one is selected.
2. If one of $r_{i-1/2}$ and $r_{i+1/2}$ is negative, the negative one is selected.
3. If both are positive, the larger one is selected.

When $r_{i-1/2}$ (or $r_{i+1/2}$) is negative, it represents opposite slopes. It has been considered that we should avoid such stencil. However as shown in Section 3 (for instance, Fig. 5 (d) and (e), and Fig. 6 (d) and (e)), CSL3D and also CSL3U can deal with preexisting opposite slopes very well (see sharp edges around $x = -0.7$ and $x = 0.1$). Therefore we considered that we do not have to avoid such stencils which have negative successive gradients and designed the selector which intentionally selects such a non-smooth stencil. If we simply select a smoother stencil, numerical oscillations could not be minimized. Although we have not fully understood the mechanism of this selector (we found this selector after numerous numerical experiments), this formulation worked well in our numerical experiments as shown in Section 3. For the case of $u_{i-1/2} \geq 0$, the smoothness of CSL3D and CSL3U are evaluated by $r_{i-1/2}$ and $r_{i-3/2}$, respectively.

3 Numerical results

We validate proposed methods through various benchmark problems and compare the results with those of other CIP-CSL schemes.

3.1 Sine wave propagation

The conservation equation (1) is solved with the initial condition $\phi(x,0) = \sin(2\pi x)$. The domain $[0,1]$, $u(x) = 1$ and periodic boundary conditions are used. Four different grid sizes (N = 100, 200, 400 and 800) are used with $\Delta t = 0.4\Delta x$ and $\Delta x = 1/N$. Errors are defined as follows

$$L_1 = \frac{1}{N}\sum_{i=1}^{N} |\phi_i - \phi_{exact,i}|, \tag{33}$$

$$L_\infty = \max(|\phi_i - \phi_{exact,i}|). \tag{34}$$

Table 1 shows the numerical results. CSL2 has 3rd-order accuracy, and CSL3H, CSL3D and CSL3U have 4th-order accuracy. Although CSL3H is the most accurate in this test, CSL3H uses a wider stencil than all others. CSL3CW is less accurate than all others due to the slop limiter. CSL3ENO approximately has 4th-order accuracy for L_1 and 3rd-order for L_∞.

Table 1: L_1 and L_∞ errors in sine wave propagation at t=1.

Method	N	L_1 error	L_1 order	L_∞ error	L_∞ order
CSL2	100	6.28×10^{-6}	-	9.86×10^{-6}	-
	200	7.85×10^{-7}	3.00	1.23×10^{-6}	3.00
	400	9.82×10^{-8}	3.00	1.54×10^{-7}	3.00
	800	1.23×10^{-8}	3.00	1.93×10^{-8}	3.00
CSL3CW	100	5.85×10^{-4}	-	5.04×10^{-3}	-
	200	1.18×10^{-4}	2.31	1.80×10^{-3}	1.49
	400	2.29×10^{-5}	2.36	6.27×10^{-4}	1.52
	800	4.57×10^{-6}	2.33	2.14×10^{-4}	1.55
CSL3H	100	8.33×10^{-8}	-	1.23×10^{-7}	-
	200	4.56×10^{-9}	4.19	6.94×10^{-9}	4.15
	400	2.72×10^{-10}	4.07	4.21×10^{-10}	4.04
	800	1.61×10^{-11}	4.02	2.61×10^{-11}	4.01
CSL3D	100	1.07×10^{-7}	-	1.68×10^{-7}	-
	200	6.68×10^{-9}	4.00	1.05×10^{-8}	4.00
	400	4.18×10^{-10}	4.00	6.56×10^{-10}	4.00
	800	2.61×10^{-11}	4.00	4.10×10^{-11}	4.00
CSL3U	100	9.13×10^{-8}	-	1.43×10^{-7}	-
	200	5.71×10^{-9}	4.00	8.97×10^{-9}	3.99
	400	3.57×10^{-10}	4.00	5.60×10^{-10}	4.00
	800	2.23×10^{-11}	4.00	3.50×10^{-11}	4.00
CSL3ENO	100	2.26×10^{-7}	-	2.47×10^{-6}	-
	200	1.54×10^{-8}	3.88	2.89×10^{-7}	3.10
	400	1.01×10^{-9}	3.93	3.33×10^{-8}	3.13
	800	6.70×10^{-11}	3.91	3.80×10^{-9}	3.13

3.2 Complex wave propagation

We validate proposed CSL schemes through Jiang-Shu complex wave propagation problem [10]. $u(x) = 1$, the domain $[-1,1]$, $N = 200$, $\Delta t = 0.4\Delta x$, $\Delta x = 2/N$, and periodic boundary conditions are used in this test. The initial condition is given as

$$\phi(x,0) = \begin{cases} \frac{1}{6}(G(x,\beta,z-\delta)+G(x,\beta,z+\delta)+4G(x,\beta,z)) & \text{if} \quad -0.8 \le x < -0.6 \\ 1 & \text{if} \quad -0.4 \le x < -0.2 \\ 1-|10(x-0.1)| & \text{if} \quad 0.0 \le x < 0.2 \\ \frac{1}{6}(F(x,\alpha,a-\delta)+F(x,\alpha,a+\delta)+4F(x,\alpha,a)) & \text{if} \quad 0.4 \le x < 0.6 \\ 0 & \text{otherwise,} \end{cases} \tag{35}$$

where

$$G(x,\beta,z) = e^{-\beta(x-z)^2}, \tag{36}$$

$$F(x,\alpha,a) = \sqrt{\max(1-\alpha^2(x-a)^2,0)}, \tag{37}$$

here $a = 0.5$, $z = -0.7$, $\delta = 0.005$, $\alpha = 10$ and $\beta = \log(2)/(36\delta^2)$.

Fig. 5 shows the results at t=16 (8 periods: 4000 time steps). CSL2, CSL3H, CSL3D and CSL3U

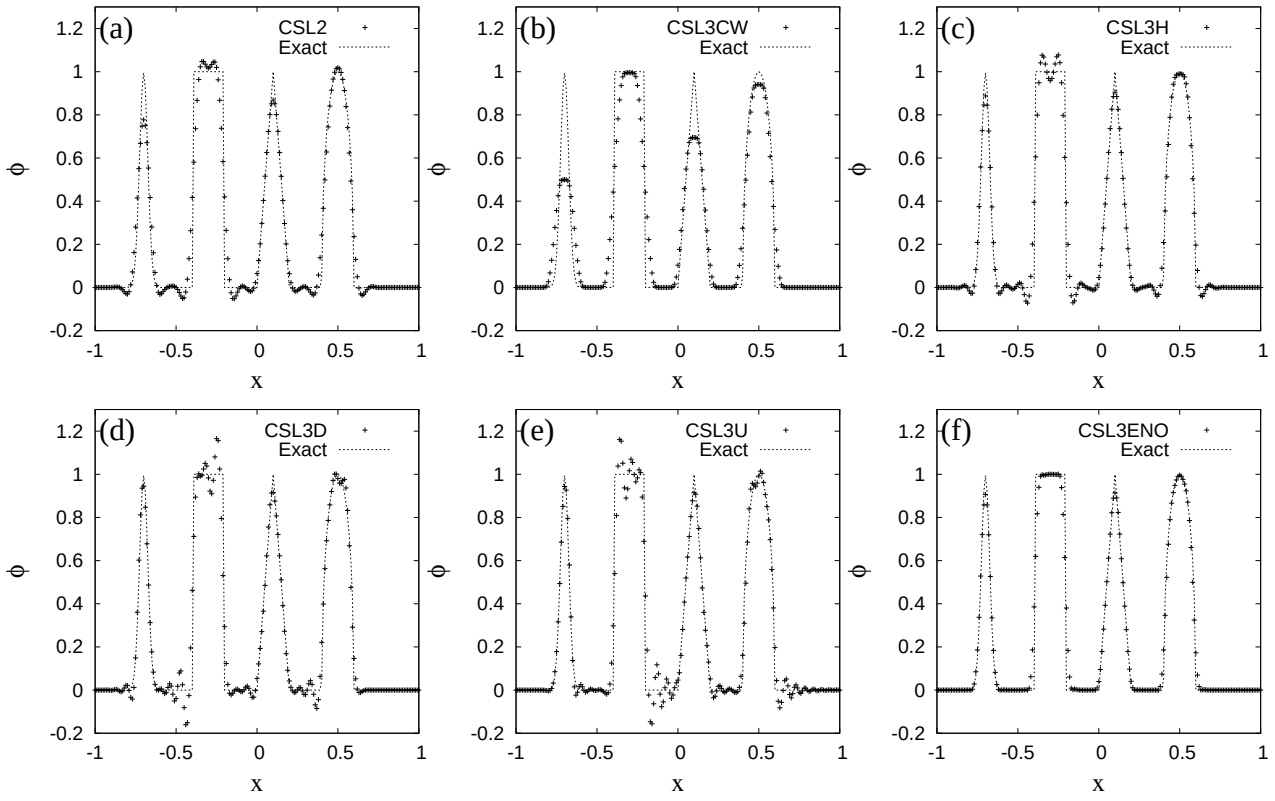

Figure 5: Numerical results of complex wave propagation test at t=16 (8 periods: 4,000 time steps). N=200 and CFL=0.4 are used.

are oscillatory around discontinuities. CSL3U generates larger numerical oscillations around discontinuities when discontinuities appear in the upwind side. The trend is opposite to CSL3D due to the nature of CSL3U and CSL3D (i.e. CSL3U and CSL3D use an additional moment in upwind and downwind sides, respectively). Although CSL3CW prevents numerical oscillations, the results are diffusive. CSL3ENO minimizes

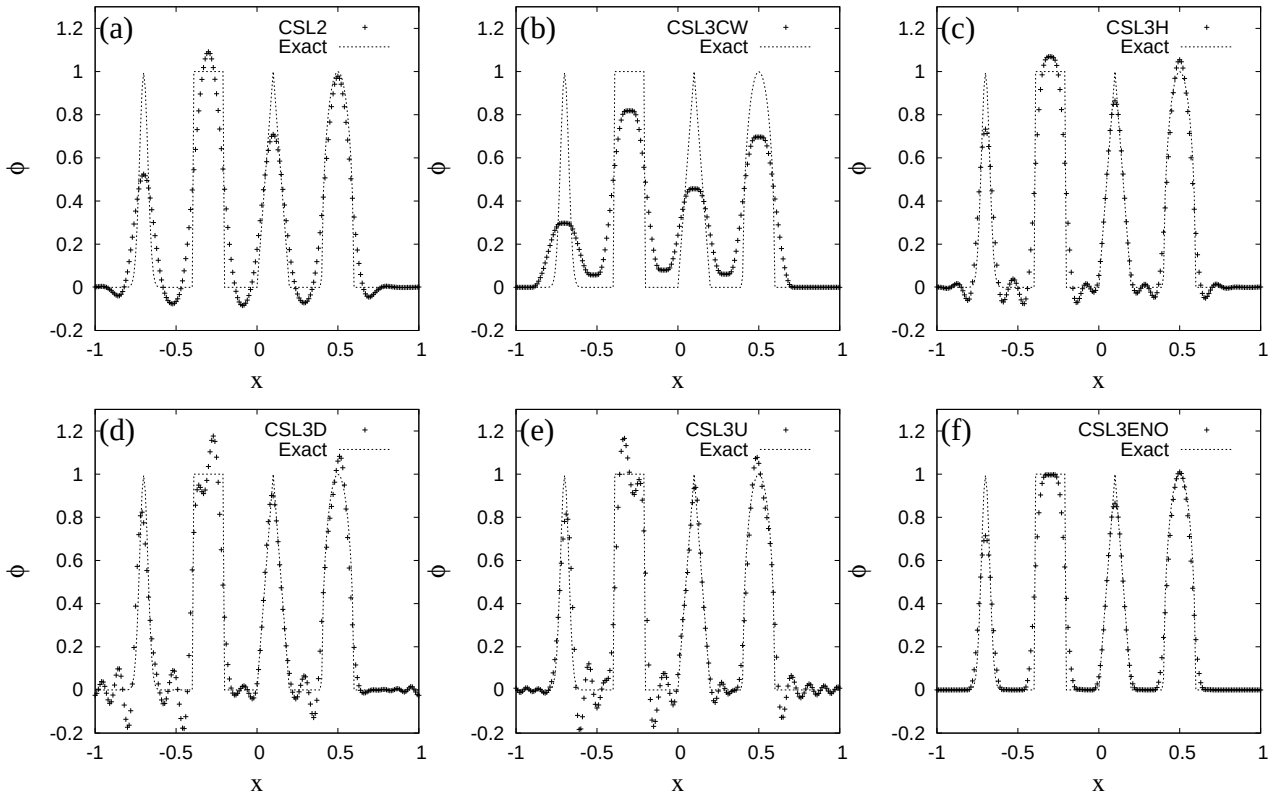

Figure 6: Numerical results of complex wave propagation test at t=160 (80 periods: 40,000 time steps). N=200 and CFL=0.4 are used.

numerical oscillations with minimum numerical diffusion. Fig. 6 shows the results at t=160 (80 periods: 40,000 time steps). Even after 40,000 time steps, CSL3ENO captures discontinuities and cusps well without numerical oscillation. Table 2 shows L_1 and L_∞ errors. In this test, CSL3ENO is consistently superior to all

Table 2: L_1 and L_∞ errors in the complex wave propagation test at t=16 (8 periods: 4000 time steps) and t=160 (80 periods: 40,000 time steps). N=200 and CFL=0.4 are used.

	4000 time steps		40,000 time steps	
	L_1 error	L_∞ error	L_1 error	L_∞ error
CSL2	4.32×10^{-2}	4.22×10^{-1}	9.28×10^{-2}	4.70×10^{-1}
CSL3CW	6.49×10^{-2}	4.94×10^{-1}	1.49×10^{-1}	6.97×10^{-1}
CSL3H	3.39×10^{-2}	3.97×10^{-1}	5.63×10^{-2}	4.35×10^{-1}
CSL3D	3.34×10^{-2}	4.60×10^{-1}	6.62×10^{-2}	5.50×10^{-1}
CSL3U	3.68×10^{-2}	4.66×10^{-1}	6.56×10^{-2}	5.45×10^{-1}
CSL3ENO	2.30×10^{-2}	3.86×10^{-1}	4.43×10^{-2}	4.31×10^{-1}

other CSL schemes.

Here we compare numerical results by the CIP-CSL3ENO scheme with numerical results by a standard WENO scheme (WENO-Roe5) [10], the 5th-order multi-memnt WENO scheme [5] and the MCV-WENO scheme [20]. In these comparisons, we obtained data by other schemes from these papers using a software (GetData Graph Digitizer). Fig. 7 shows a comparison of numerical results by WENO-Roe5 and the CIP-CSL3ENO scheme in complex wave propagation test at t=8. The CSL-CSL3ENO scheme is less diffusive

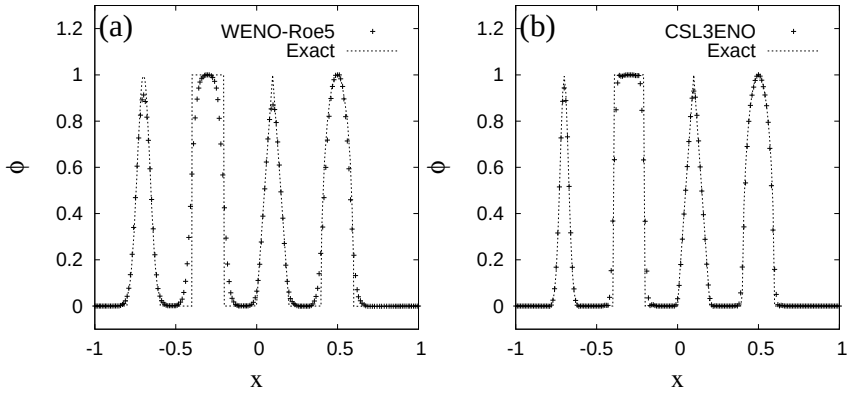

Figure 7: A comparison of numerical results by WENO-Roe5 [10] and the CIP-CSL3ENO scheme in complex wave propagation test at t=8 (4 periods: 2,000 time steps). N=200 and CFL=0.4 are used.

than WENO-Roe5. Fig. 8 shows a comparison of numerical results by the multi-moment WENO scheme [5], the MCV-WENO scheme [20] and the CIP-CSL3ENO scheme, in complex wave propagation test at t=2 (Note: The time is different with the previous comparison in Fig. 7). The result shows that the CIP-CSL3ENO scheme is less diffusive than the multi-moment WENO scheme and the MCV-WENO scheme.

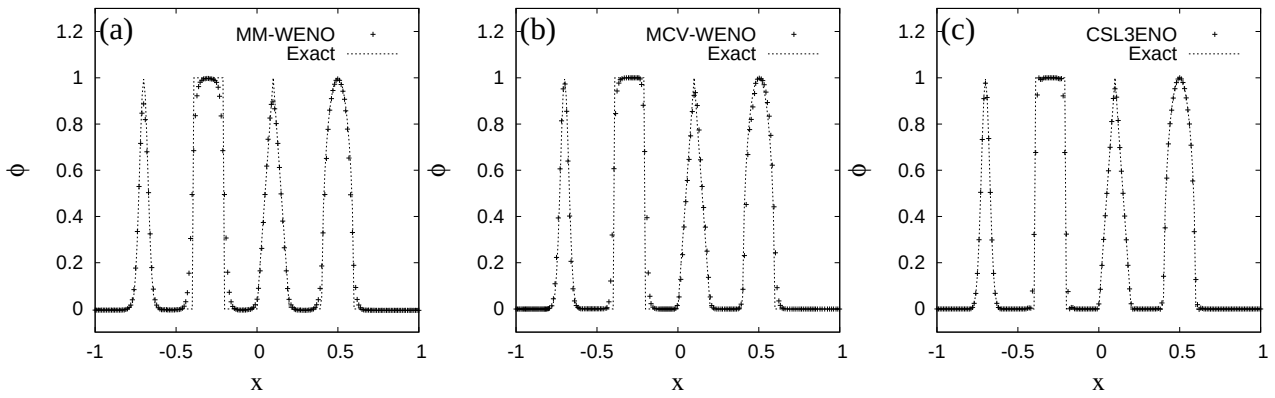

Figure 8: A comparison of numerical results by multi-moment WENO schemes and the CIP-CSL3ENO scheme in complex wave propagation test at t=2 (1 period: 500 time steps). N=200 and CFL=0.4 are used.

3.3 Square wave propagation

Here we would like to show numerical results of square wave propagation by CSL3D, CSL3U and CSL3ENO using different CFL numbers because CSL3D and CSL3U show different behaviors depending on the CFL number. $u(x) = 1$, the domain $[-1,1]$, $N = 200$, $\Delta x = 2/N$, and periodic boundary conditions are used in this test. The initial condition is given as

$$\phi(x,0) = \begin{cases} 1 & \text{if} \quad -0.3 \le x < 0.3 \\ 0 & \text{otherwise.} \end{cases} \tag{38}$$

In this test, CFL=0.2 and 0.8 ($\Delta t = 0.2\Delta x$ and $0.8\Delta x$) are used. Figures 9 and 10 show numerical results of CFL=0.2 and CFL0.8, respectively. As shown in these numerical results, when the CFL number is 0.2

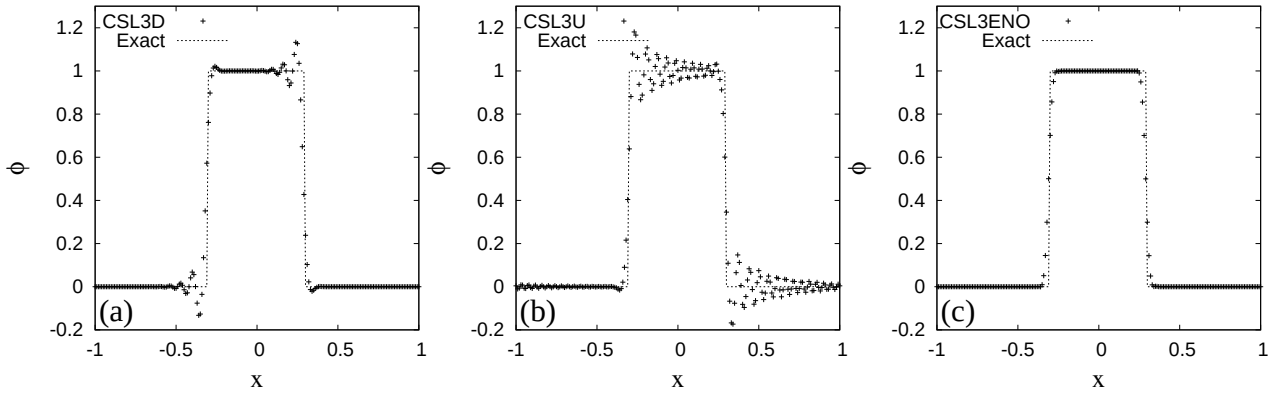

Figure 9: Numerical results of square wave propagation test at t=16 (8,000 time steps). N=200 and CFL=0.2 are used.

(less than 0.5), CSL3U has larger numerical oscillation than that of CSL3D as shown in Fig. 9. On the other hand, the CFL number is 0.8 (larger than 0.5), CSL3D has larger numerical oscillation. These are because when CFL<0.5, the departure point is closer to the additional moment of CSL3D (i.e. $\hat{\phi}_{i-1}$ in Fig. 1). When CFL>0.5, the departure point is closer to the additional moment of CSL3U (i.e. $\hat{\phi}_{i+1}$ in Fig. 1). This trend is consistent with the result of Fourier analysis as shown in Section 2.4.2. CSL3ENO can deal with different CFL numbers as shown in figures 9 (c) and 10 (c).

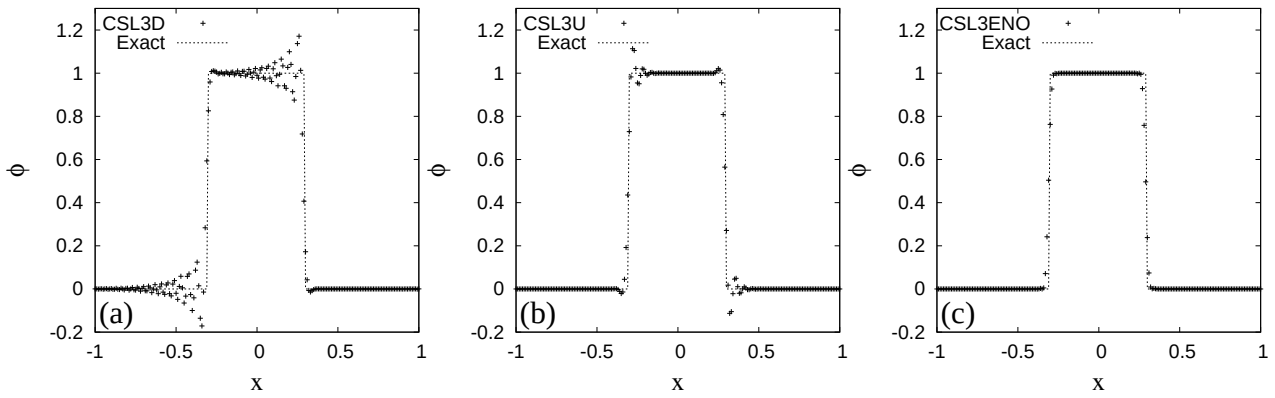

Figure 10: Numerical results of square wave propagation test at t=16 (2,000 time steps). N=200 and CFL=0.8 are used.

3.4 Capturing extrema of various smoothness

In capturing extrema of various smoothness test [3], the initial condition is given as

$$\phi(x+0.5,0) = \begin{cases} -x\sin(1.5\pi x^2) & \text{if} \quad -1 \le x < -1/3 \\ |\sin(2\pi x)| & \text{if} \quad |x| \le 1/3 \\ 2x-1-\sin(3\pi x)/6 & \text{otherwise,} \end{cases} \tag{39}$$

for $-1 \le x \le 1$. $u(x) = 1$, $N = 100$, CFL = 0.4 and periodic boundary conditions are used. Fig. 11 shows the numerical results at $t = 8$ (4 periods). CSL3ENO captures discontinuities and smooth profiles without numerical oscillations. Although other 4th-order CSL3 schemes (CSL3H, CSL3D and CSL3U) capture discontinuities, these schemes are not oscillation free around the discontinuities. CSL3U has numerical oscillations not only around discontinuities but also smooth regions as shown in Fig. 11 (e). The numerical oscillations in smooth regions will be the same type of oscillations which appear in the square wave propagation test as discussed in Section 3.3. Table 3 shows L_1 and L_∞ errors. CSL3ENO is superior to all others

Table 3: Errors in capturing extrema of various smoothness test at t=8. N=100 and CFL=0.4 are used.

	L_1 error	L_∞ error
CSL2	6.29×10^{-2}	7.85×10^{-1}
CSL3CW	1.12×10^{-1}	8.84×10^{-1}
CSL3H	6.00×10^{-2}	7.53×10^{-1}
CSL3D	5.73×10^{-2}	8.41×10^{-1}
CSL3U	6.34×10^{-2}	8.52×10^{-1}
CSL3ENO	4.13×10^{-2}	7.24×10^{-1}

CSL schemes in this test.

3.5 Burgers' equation

In this test, we solve the inviscid Burgers' equation in its conservative formulation

$$\frac{\partial u}{\partial t} + \frac{\partial (u^2/2)}{\partial x} = 0, \tag{40}$$

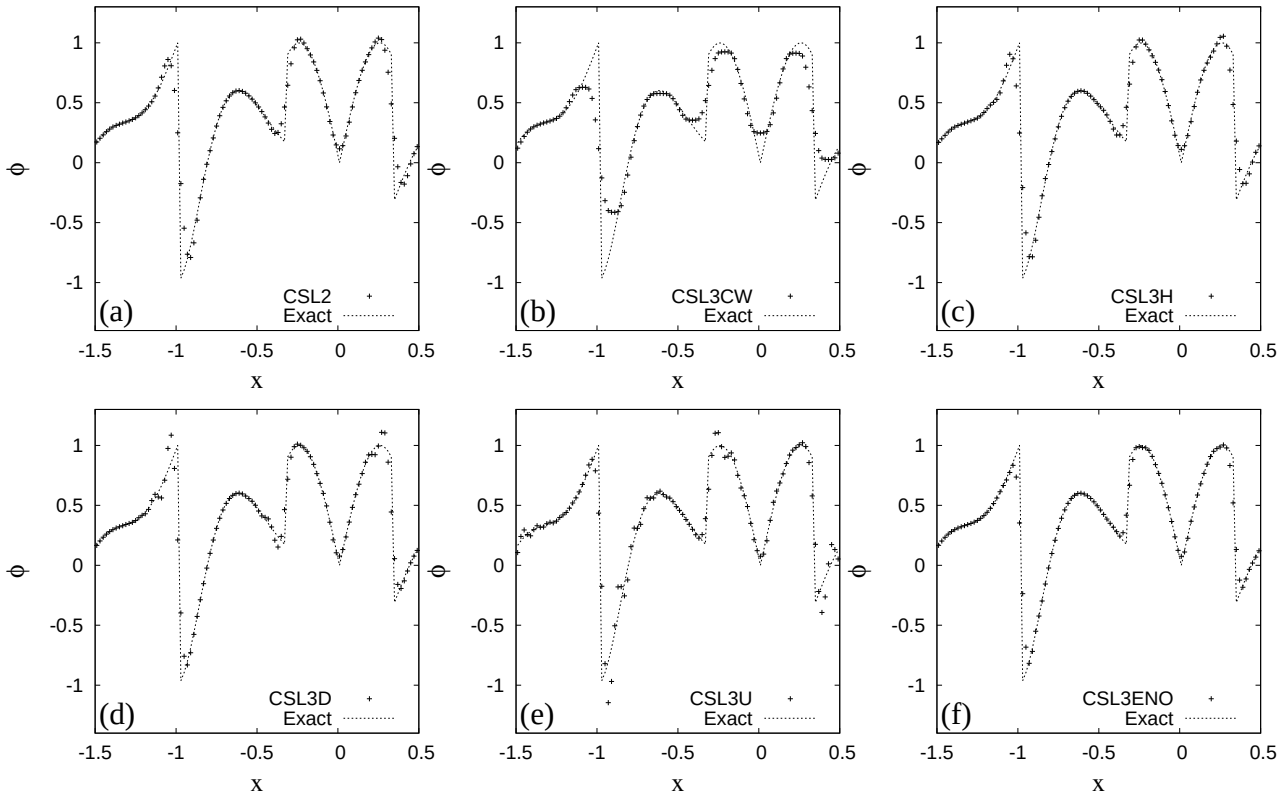

Figure 11: Numerical results of capturing extrema of various smoothness test at t=8. N=100 and CFL=0.4 are used.

with the initial condition $u(x,0) = 0.5 + 0.4\cos(2\pi x)$. $N = 200$, CFL = 0.2 and periodic boundary conditions are used. Fig. 12 shows the results at t=1. The reference solution is created by using CSL3CW with N = 10,000. CSL2, CSL3H, CSL3D and CSL3U have numerical oscillation around the discontinuity. Although

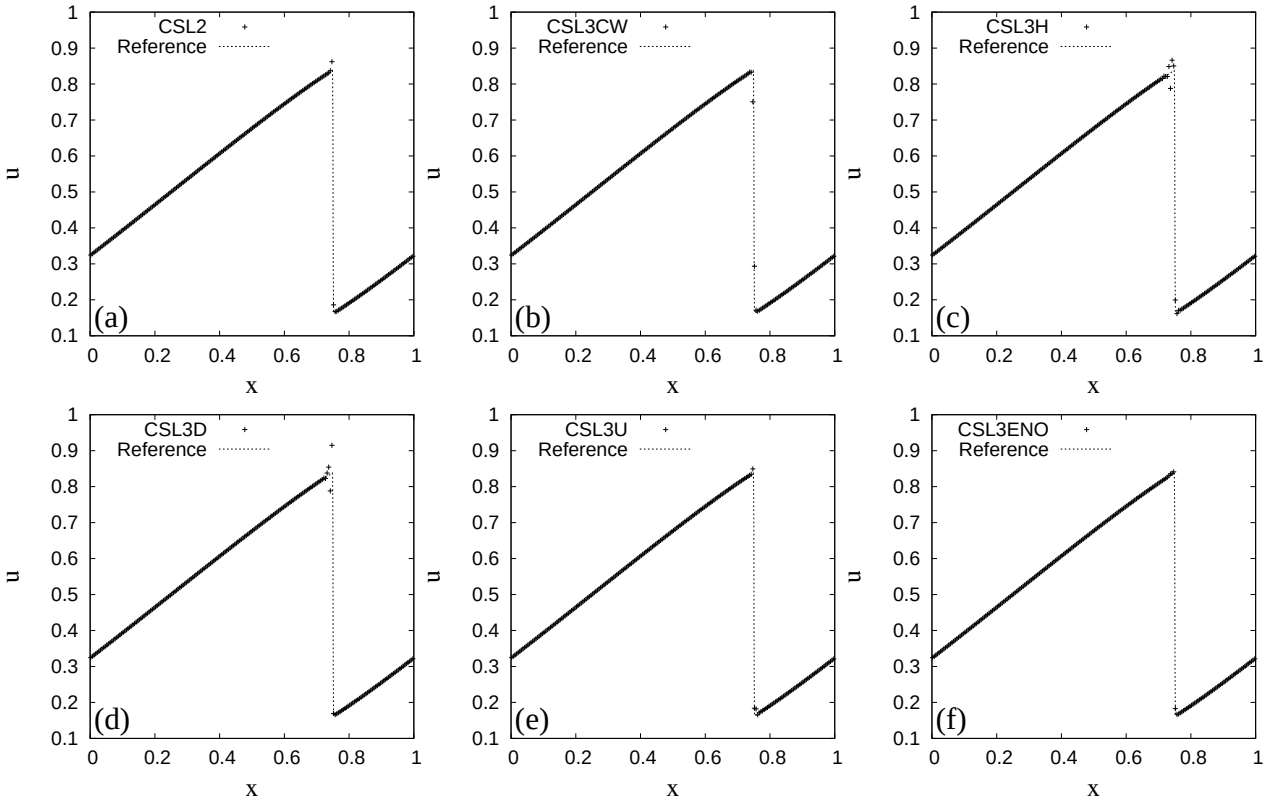

Figure 12: Numerical results of Burgers' equation at t=1. N=200 and CFL=0.2 are used.

both CSL3CW and CSL3ENO have no oscillation around the discontinuity, CSL3ENO is less diffusive than CSL3CW.

Table 4 shows errors of CSL3D, CSL3U and CSL3ENO schemes at t=0.25 (before the shock is formed). CSL3D, CSL3U and CSL3ENO approximately have 4th-order accuracy in this test.

3.6 Sod's problem

Hereafter we test the proposed schemes through compressible fluid problems using the third-order Runge-Kutta characteristic formulation [7]. Firstly we test the proposed schemes using Sod's problem [19]. The initial condition is

$$\begin{array}{llll} \rho(x,0) = 1; & u(x,0) = 0; & p(x,0) = 1; & \text{if } x < 0.5 \\ \rho(x,0) = 0.125; & u(x,0) = 0; & p(x,0) = 0.1; & \text{otherwise,} \end{array} \tag{41}$$

where ρ is the density and p is pressure. $N = 200$ and CFL = 0.2 are used in this test. Fig. 13 shows the numerical results. CSL2, CSL3H, CSL3D and CSL3U have numerical oscillations around the discontinuities. Although both CSL3CW and CSL3ENO have no oscillation around the discontinuities, CSL3ENO is less diffusive than CSL3CW.

Table 4: L_1 and L_∞ errors in Burgers' equation at t=0.25.

Method	N	L_1 error	L_1 order	L_∞ error	L_∞ order
CSL3D	100	6.61×10^{-8}	-	3.97×10^{-7}	-
	200	4.52×10^{-9}	3.87	2.84×10^{-8}	3.81
	400	2.97×10^{-10}	3.93	2.00×10^{-9}	3.83
	800	2.32×10^{-11}	3.68	1.76×10^{-10}	3.51
CSL3U	100	3.88×10^{-8}	-	2.35×10^{-7}	-
	200	2.48×10^{-9}	3.97	1.50×10^{-8}	3.97
	400	1.59×10^{-10}	3.96	9.20×10^{-10}	4.03
	800	1.11×10^{-11}	3.84	5.74×10^{-11}	4.00
CSL3ENO	100	5.16×10^{-8}	-	2.78×10^{-7}	-
	200	3.56×10^{-9}	3.86	2.01×10^{-8}	3.79
	400	2.32×10^{-10}	3.94	1.39×10^{-9}	3.85
	800	1.39×10^{-11}	4.06	8.08×10^{-11}	4.10

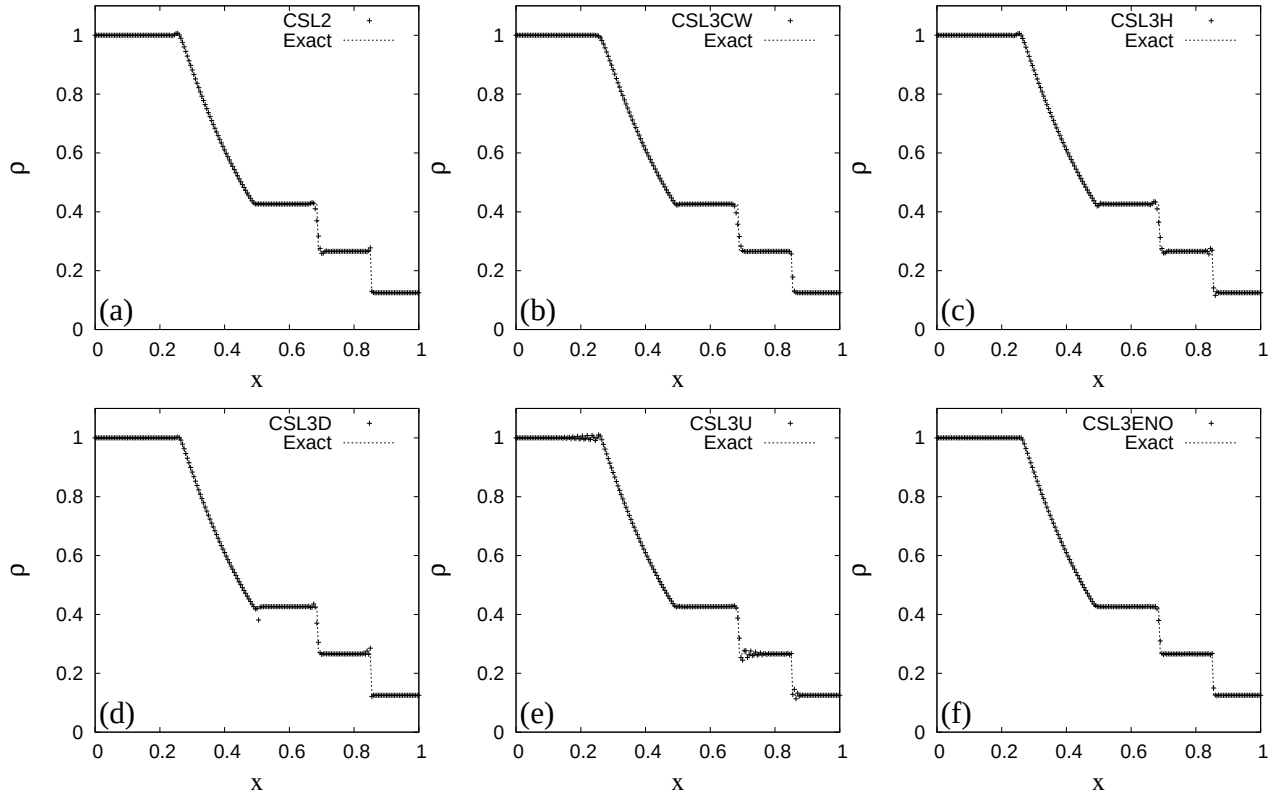

Figure 13: Numerical results of Sod's shock tube problem at t = 0.2 (CFL=0.2 and N=200).

3.7 Lax's problem

We validate the proposed schemes using Lax's problem which includes a discontinuity in the velocity initial condition, while Sod's problem does not include the discontinuity. The initial condition

$$\begin{array}{llll} \rho(x,0) = 0.445; & u(x,0) = 0.698; & p(x,0) = 3.528; & \text{if } x < 0.5 \\ \rho(x,0) = 0.5; & u(x,0) = 0; & p(x,0) = 0.571; & \text{otherwise,} \end{array} \tag{42}$$

$N = 200$ and CFL = 0.2 are used. Fig. 14 shows the numerical result at t=0.12. CSL2, CSL3H, CSL3D and

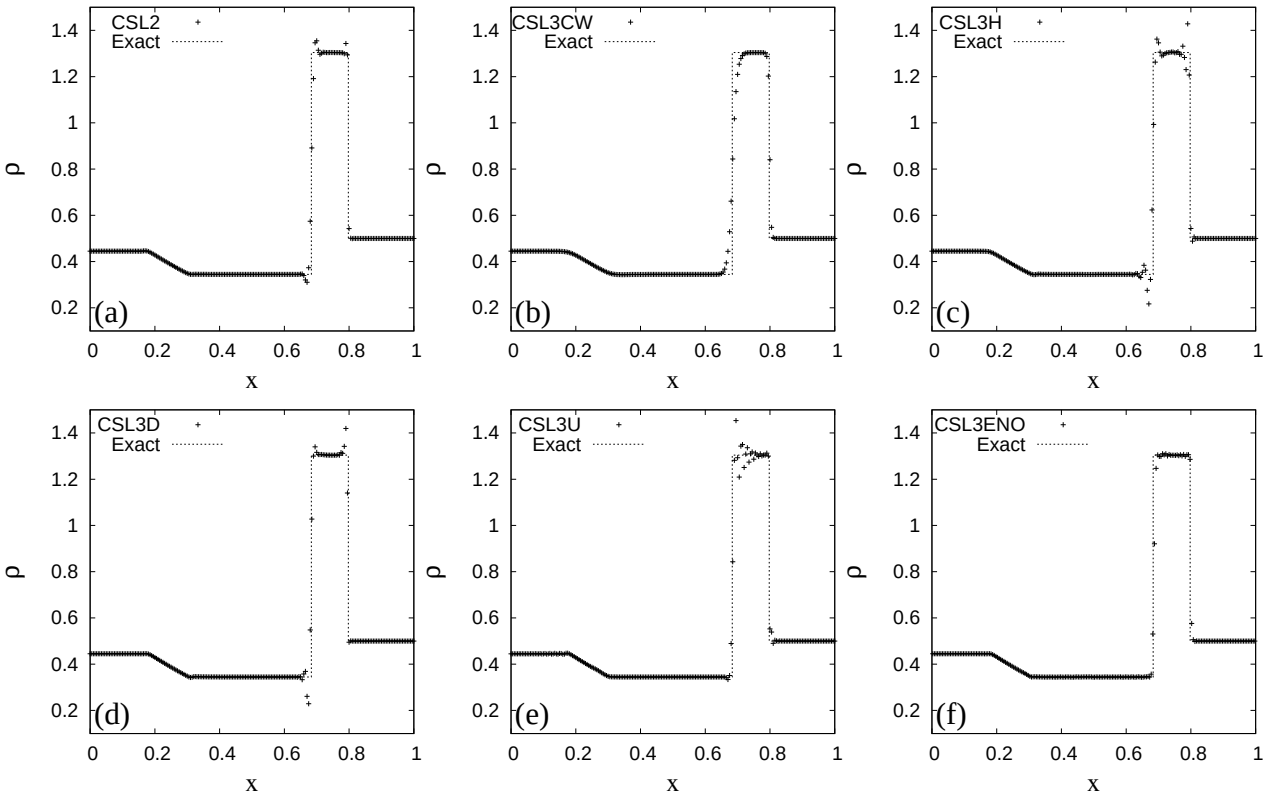

Figure 14: Numerical results of Lax's shock tube problem at t=0.12 (CFL=0.2 and N=200).

CSL3U have numerical oscillations around the discontinuities and CSL3CW is diffusive at discontinuities (especially the contact discontinuity). CSL3ENO captures the contact discontinuity as well as the shock well without numerical oscillations.

3.8 3D free surface flow (droplet-droplet interaction)

In this subsection, we show a numerical result of two droplets interaction by the CIP-CSL3ENO scheme, and compare the result with the experiment (We=40 in [1]) and the result by the CIP-CSLR scheme [26] which has similar capability with the CIP-CSL3CW scheme (CSLR can be considered as a less oscillator CSL scheme for incompressible flows). In this comparison, the CIP-CSL3ENO scheme was used only for the momentum equation. The CIP-CSL3ENO scheme employs the same moments with other CIP-CSL schemes (i.e. cell average and boundary value). Therefore basically we can use the CIP-CS3ENO scheme in any codes which are based on a CIP-CSL scheme by just replacing the CIP-CSL scheme to the CIP-CSL3ENO scheme. Here we show a numerical result of two droplets collision/separation based on a well validated free surface flow framework [28, 29, 30, 31].

Fig. 15 shows the numerical result. In these simulations, $\Delta x = \Delta y = \Delta z = D/13$ (D is the initial droplet

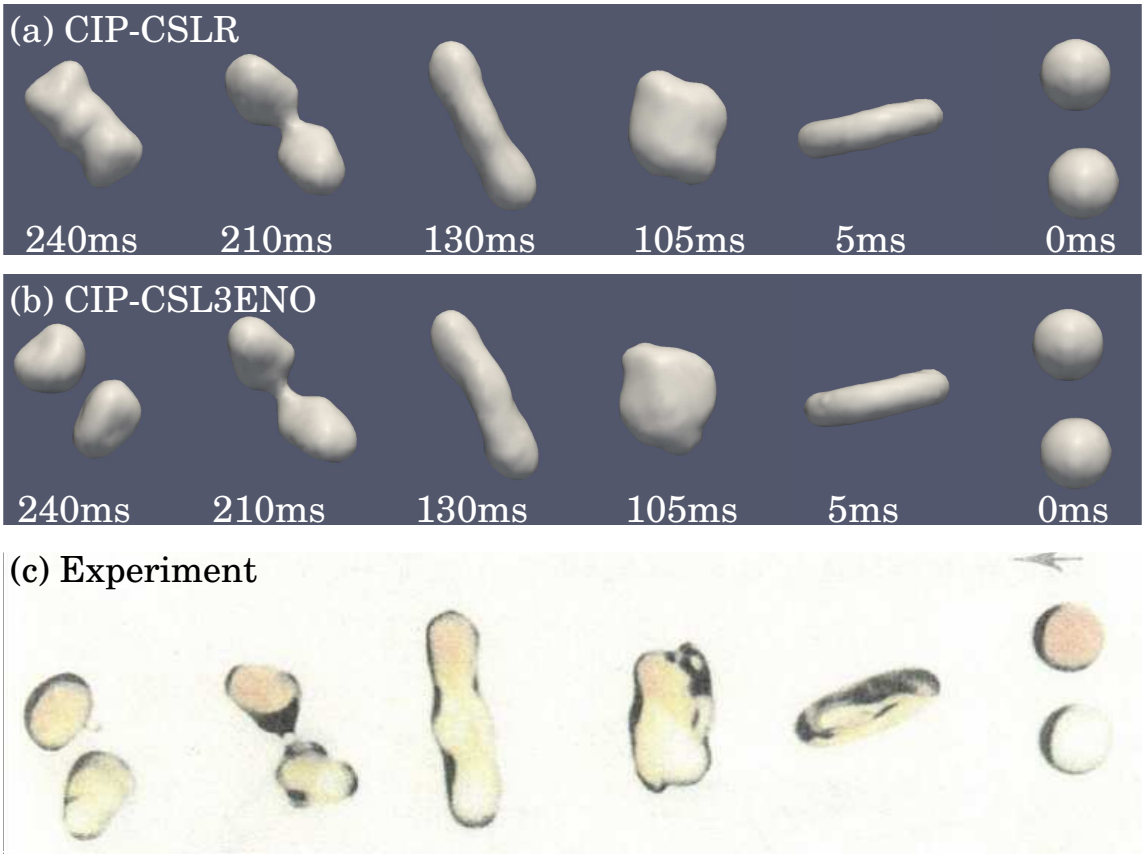

Figure 15: Numerical results of droplet-droplet collision/separation by the CIP-CSLR scheme (a) and CIP-CSL3ENO schemes (b) with the experiment (c) [1]. $\Delta x = \Delta y = \Delta z = D/13$ and $64 \times 64 \times 64$ Cartesian grid are used.

diameter) and $64 \times 64 \times 64$ Cartesian grid are used. While CSL3ENO captures the droplet separation as well as collision, CSLR fails to capture the droplet separation with this numerical resolution. This will be due to the larger numerical diffusion by CSLR. However if the resolution is increased, CSLR also captures the droplet separation [31].

4 Conclusions

We proposed the CIP-CSL3ENO scheme which is based on the CIP-CSL3D scheme and newly proposed CIP-CSL3U scheme. We also proposed the ENO indicator for the multi-moment framework, which intentionally selects non-smooth stencil but can efficiently minimize numerical oscillations. The CIP-CSL3ENO scheme approximately has 4th-order accuracy for the sine wave propagation test, and captures discontinuities and smooth solutions without numerical oscillations in various test problems. The numerical results of two droplets collision/separation show that the CIP-CSL3ENO scheme can be applied to various types of fluid problems not only compressible flow problems but also incompressible and 3D free surface flow problems.

5 Acknowledgments

This research was supported in part by FLEXIS which is part-funded by the European Regional Development Fund (ERDF), through the Welsh Government. The numerical simulations were partially conducted on computers at Center for Earth Information Science and Technology in JAMSTEC, at Yukawa Institute of Theoretical Physics in Kyoto University and at HPC Wales.

A Mathematical formulations of Fourier analysis of CSL3U and CSL3D

The following equations are mathematical formulations of Fourier analysis which are given in Section 2.4.2. Φ_x, Φ_{xx} and Φ_{xxx} represent the first derivative of Φ, second derivative and third derivative, respectively.
The spatial derivatives of CSL3U at x_i in Fourier space:

$$\begin{aligned}\Phi_x(w) = \frac{1}{12}\left(\cos(\frac{3w}{2}) + 23\cos(\frac{w}{2}) - \frac{30}{w}\sin(\frac{w}{2}) - \frac{6}{w}\sin(\frac{3w}{2})\right) \\ + \left(\sin(\frac{3w}{2}) + 33\sin(\frac{w}{2}) + \frac{6}{w}\cos(\frac{3w}{2}) - \frac{6}{w}\cos(\frac{w}{2})\right) j,\end{aligned} \tag{43}$$

$$\Phi_{xx}(w) = \left(12\cos(\frac{w}{2}) - \frac{24}{w}\sin(\frac{w}{2})\right), \tag{44}$$

$$\begin{aligned}\Phi_{xxx}(w) = \left(-\cos(\frac{3w}{2}) - 23\cos(\frac{w}{2}) + \frac{30}{w}\sin(\frac{w}{2}) + \frac{6}{w}\sin(\frac{3w}{2})\right) \\ - \left(\sin(\frac{3w}{2}) + 9\sin(\frac{w}{2}) + \frac{6}{w}\cos(\frac{3w}{2}) - \frac{6}{w}\cos(\frac{w}{2})\right) j.\end{aligned} \tag{45}$$

The spatial derivatives of CSL3D at x_i in Fourier space:

$$\begin{aligned}\Phi_x(w) = \frac{1}{12}\left(-\cos(\frac{3w}{2}) - 23\cos(\frac{w}{2}) + \frac{30}{w}\sin(\frac{w}{2}) + \frac{6}{w}\sin(\frac{3w}{2})\right) \\ + \left(\sin(\frac{3w}{2}) + 33\sin(\frac{w}{2}) + \frac{6}{w}\cos(\frac{3w}{2}) - \frac{6}{w}\cos(\frac{w}{2})\right) j,\end{aligned} \tag{46}$$

$$\Phi_{xx}(w) = \left(12\cos(\frac{w}{2}) - \frac{24}{w}\sin(\frac{w}{2})\right), \tag{47}$$

$$\begin{aligned}\Phi_{xxx}(w) = \left(\cos(\frac{3w}{2}) + 23\cos(\frac{w}{2}) - \frac{30}{w}\sin(\frac{w}{2}) - \frac{6}{w}\sin(\frac{3w}{2})\right) \\ - \left(\sin(\frac{3w}{2}) + 9\sin(\frac{w}{2}) + \frac{6}{w}\cos(\frac{3w}{2}) - \frac{6}{w}\cos(\frac{w}{2})\right) j.\end{aligned} \tag{48}$$

The spatial derivatives of CSL3U at $x_{i-1/2}$ in Fourier space:

$$\Phi_x(w) = \left(-\frac{31}{6} - \frac{14}{3}\cos(w) + \frac{8}{w}\sin(w) + \frac{1}{w}\sin(2w) - \frac{1}{6}\cos(2w) \right) + \left(-\frac{14}{3}\sin(w) - \frac{8}{w}\cos(w) + \frac{9}{w} - \frac{1}{w}\cos(2w) - \frac{1}{6}\sin(2w) \right) j, \tag{49}$$

$$\Phi_{xx}(w) = \left(13 + 22\cos(w) - \frac{24}{w}\sin(w) - \frac{6}{w}\sin(2w) + \cos(2w) \right) + \left(22\sin(w) - \frac{30}{w} + \frac{24}{w}\cos(w) + \frac{6}{w}\cos(2w) + \sin(2w) \right) j, \tag{50}$$

$$\Phi_{xxx}(w) = \left(-14 - 32\cos(w) + \frac{24}{w}\sin(w) + \frac{12}{w}\sin(2w) - 2\cos(2w) \right) + \left(-32\sin(w) + \frac{36}{w} - \frac{24}{w}\cos(w) - \frac{12}{w}\cos(2w) - 2\sin(2w) \right) j. \tag{51}$$

The spatial derivatives of CSL3D at $x_{i-1/2}$ in Fourier space:

$$\Phi_x(w) = \left(-\frac{2}{3}\cos(w) + \frac{2}{w}\sin(w) - \frac{4}{3} \right) + \left(-\sin(w) + \frac{4}{w} - \frac{4}{w}\cos(w) \right) j, \tag{52}$$

$$\Phi_{xx}(w) = -2\cos(w) + \frac{12}{w}\sin(w) - 10, \tag{53}$$

$$\Phi_{xxx}(w) = \left(16\cos(w) - \frac{48}{w}\sin(w) + 32 \right) + \left(12\sin(w) + \frac{24}{w}\cos(w) - \frac{24}{w} \right) j. \tag{54}$$

The spatial derivatives of CSL3U at $x_{x+1/2}$ in Fourier space:

$$\Phi_x(w) = -\left(-\frac{2}{3}\cos(w) + \frac{2}{w}\sin(w) - \frac{4}{3} \right) + \left(-\sin(w) + \frac{4}{w} - \frac{4}{w}\cos(w) \right) j, \tag{55}$$

$$\Phi_{xx}(w) = -2\cos(w) + \frac{12}{w}\sin(w) - 10, \tag{56}$$

$$\Phi_{xxx}(w) = -\left(16\cos(w) - \frac{48}{w}\sin(w) + 32 \right) + \left(12\sin(w) + \frac{24}{w}\cos(w) - \frac{24}{w} \right) j. \tag{57}$$

The spatial derivatives of CSL3D at $x_{x+1/2}$ in Fourier space:

$$\Phi_x(w) = -\left(-\frac{31}{6} - \frac{14}{3}\cos(w) + \frac{8}{w}\sin(w) + \frac{1}{w}\sin(2w) - \frac{1}{6}\cos(2w) \right) + \left(-\frac{14}{3}\sin(w) - \frac{8}{w}\cos(w) + \frac{9}{w} - \frac{1}{w}\cos(2w) - \frac{1}{6}\sin(2w) \right) j, \tag{58}$$

$$\Phi_{xx}(w) = \left(13 + 22\cos(w) - \frac{24}{w}\sin(w) - \frac{6}{w}\sin(2w) + \cos(2w)\right) \tag{59}$$
$$-\left(22\sin(w) - \frac{30}{w} + \frac{24}{w}\cos(w) + \frac{6}{w}\cos(2w) + \sin(2w)\right) j,$$

$$\Phi_{xxx}(w) = -\left(-14 - 32\cos(w) + \frac{24}{w}\sin(w) + \frac{12}{w}\sin(2w) - 2\cos(2w)\right) \tag{60}$$
$$+\left(-32\sin(w) + \frac{36}{w} - \frac{24}{w}\cos(w) - \frac{12}{w}\cos(2w) - 2\sin(2w)\right) j.$$

References

[1] N. Ashgriz and J. Y. Poo. Coalescence and separation in binary collisions of liquid drops. *Journal of Fluid Mechanics*, 221:183–204, 12 1990.

[2] P. Colella and P. R. Woodward. The piecewise parabolic method (PPM) for gas-dynamical simulations. *Journal of Computational Physics*, 54(1):174 – 201, 1984.

[3] A. Harten, B. Engquist, S. Osher, and S. R. Chakravarthy. Uniformly high order accurate essentially non-oscillatory schemes, III. *Journal of Computational Physics*, 71(2):231 – 303, 1987.

[4] G. Hu, R. Li, and T. Tang. A robust WENO type finite volume solver for steady euler equations on unstructured grids. *Communications in Computational Physics*, 9(3):627 – 648, 2011.

[5] C.-S. Huang, F. Xiao, and T. Arbogast. Fifth order multi-moment weno schemes for hyperbolic conservation laws. *Journal of Scientific Computing*, 64(2):477–507, 2015.

[6] J. M. Hyman. Accurate monotonicity preserving cubic interpolation. *SIAM Journal on Scientific and Statistical Computing*, 4(4):645–654, 1983.

[7] S. Ii and F. Xiao. CIP/multi-moment finite volume method for euler equations: A semi-lagrangian characteristic formulation. *Journal of Computational Physics*, 222(2):849 – 871, 2007.

[8] S. Ii and F. Xiao. High order multi-moment constrained finite volume method. part i: Basic formulation. *Journal of Computational Physics*, 228(10):3669 – 3707, 2009.

[9] Y. Imai and T. Aoki. Accuracy study of the IDO scheme by fourier analysis. *Journal of Computational Physics*, 217(2):453 – 472, 2006.

[10] G.-S. Jiang and C.-W. Shu. Efficient implementation of weighted ENO schemes. *Journal of Computational Physics*, 126(1):202 – 228, 1996.

[11] X.-D. Liu, S. Osher, and T. Chan. Weighted essentially non-oscillatory schemes. *Journal of Computational Physics*, 115(1):200 – 212, 1994.

[12] N. Onodera, T. Aoki, and K. Yokoi. A fully conservative high-order upwind multi-moment method using moments in both upwind and downwind cells. *International Journal for Numerical Methods in Fluids*, 2016. fld.4228.

[13] J.-M. Qiu and C.-W. Shu. Conservative high order semi-lagrangian finite difference WENO methods for advection in incompressible flow. *Journal of Computational Physics*, 230(4):863 – 889, 2011.

[14] S. Serna and A. Marquina. Power ENO methods: a fifth-order accurate weighted power ENO method. *Journal of Computational Physics*, 194(2):632 – 658, 2004.

[15] C.-W. Shu. Total-variation-diminishing time discretizations. *SIAM Journal on Scientific and Statistical Computing*, 9(6):1073–1084, 1988.

[16] C.-W. Shu. *Advanced Numerical Approximation of Nonlinear Hyperbolic Equations: Lectures given at the 2nd Session of the Centro Internazionale Matematico Estivo (C.I.M.E.) held in Cetraro, Italy, June 23–28, 1997*, chapter Essentially non-oscillatory and weighted essentially non-oscillatory schemes for hyperbolic conservation laws, pages 325–432. Springer Berlin Heidelberg, Berlin, Heidelberg, 1998.

[17] C.-W. Shu and S. Osher. Efficient implementation of essentially non-oscillatory shock-capturing schemes. *Journal of Computational Physics*, 77(2):439 – 471, 1988.

[18] C.-W. Shu and S. Osher. Efficient implementation of essentially non-oscillatory shock-capturing schemes, II. *Journal of Computational Physics*, 83(1):32 – 78, 1989.

[19] G. A. Sod. A survey of several finite difference methods for systems of nonlinear hyperbolic conservation laws. *Journal of Computational Physics*, 27(1):1 – 31, 1978.

[20] Z. Sun, H. Teng, and F. Xiao. A slope constrained 4th order multi-moment finite volume method with weno limiter. *Communications in Computational Physics*, 18:901–930, 2015.

[21] R. Tanaka, T. Nakamura, and T. Yabe. Constructing exactly conservative scheme in a non-conservative form. *Computer Physics Communications*, 126(3):232 – 243, 2000.

[22] F. Xiao. Unified formulation for compressible and incompressible flows by using multi-integrated moments I: one-dimensional inviscid compressible flow. *Journal of Computational Physics*, 195(2):629 – 654, 2004.

[23] F. Xiao, R. Akoh, and S. Ii. Unified formulation for compressible and incompressible flows by using multi-integrated moments II: Multi-dimensional version for compressible and incompressible flows. *Journal of Computational Physics*, 213(1):31 – 56, 2006.

[24] F. Xiao, A. Ikebata, and T. Hasegawa. Numerical simulations of free-interface fluids by a multi-integrated moment method. *Computers and Structures*, 83(67):409 – 423, 2005. Frontier of Multi-Phase Flow Analysis and Fluid-StructureFrontier of Multi-Phase Flow Analysis and Fluid-Structure.

[25] F. Xiao and T. Yabe. Completely conservative and oscillationless semi-lagrangian schemes for advection transportation. *Journal of Computational Physics*, 170(2):498 – 522, 2001.

[26] F. Xiao, T. Yabe, X. Peng, and H. Kobayashi. Conservative and oscillation-less atmospheric transport schemes based on rational functions. *Journal of Geophysical Research: Atmospheres*, 107(D22):ACL 2–1–ACL 2–11, 2002. 4609.

[27] T. Yabe, R. Tanaka, T. Nakamura, and F. Xiao. An exactly conservative semi-lagrangian scheme (CIP-CSL) in one dimension. *Monthly Weather Review*, 129(2):332–344, 2001.

[28] K. Yokoi. A numerical method for free-surface flows and its application to droplet impact on a thin liquid layer. *Journal of Scientific Computing*, 35(2):372–396, 2008.

[29] K. Yokoi. A practical numerical framework for free surface flows based on CLSVOF method, multi-moment methods and density-scaled CSF model: Numerical simulations of droplet splashing. *Journal of Computational Physics*, 232(1):252 – 271, 2013.

[30] K. Yokoi. A density-scaled continuum surface force model within a balanced force formulation. *Journal of Computational Physics*, 278:221 – 228, 2014.

[31] K. Yokoi, R. Onishi, X.-L. Deng, and M. Sussman. Density-scaled balanced continuum surface force model with a level set based curvature interpolation technique. *International Journal of Computational Methods*, 13(04):1641004, 2016.